Unexpected band-bending of donor-doped PbZr_0.52 Ti_0.48 O_3 films

Nicholas Barrett, Ibrahima Gueye, Gwenael Le Rhun, Olivier Renault, Emmanuel Defay

Unexpected band-bending of donor-doped $PbZr_{0.52}Ti_{0.48}O_3$ films

Nicholas Barrett

SPEC, CEA, CNRS, Université Paris Saclay, F-91191 Gif-sur-Yvette, France

Ibrahima Gueye

Univ. Grenoble Alpes, CEA, LETI, F-38000, Grenoble, France

current address: Synchrotron X-ray Group, Research Center for Advanced Measurement and Characterization, National Institute for Materials Science (NIMS), 1-1-1 Kouto, Sayo, Hyogo 679-5148, Japan and Synchrotron X-ray Station at SPring-8, Research Network and Facility Services Division, NIMS, 1-1-1 Kouto, Sayo, Hyogo, Japan

Gwenael Le Rhun, Olivier Renault

Univ. Grenoble Alpes, CEA, LETI, 38000 Grenoble, France

Emmanuel Defay

Luxembourg Institute of Science and Technology, Material Research and Technology Department, 41 Rue du Brill, L-4422 Belvaux, Luxembourg

Keywords: Lead zirconate titanate, X-ray photoelectron spectroscopy, Doping, Band bending

1. Introduction

Lead zirconate titanate, $PbZr_xTi_{1-x}O_3$ (PZT) has excellent dielectric, piezoelectric and ferroelectric properties, important for a wide variety of applications such as MEMS sensors and actuators [1, 2], RF applications [3] and robust non-volatile memory cells [4]. It is a prime candidate for new generation, decoupling capacitor stacks thanks to its high dielectric constant. Industry-ready, high-quality PZT layers can be prepared by wet chemistry [5]. A full device film is usually grown as a series of sol-gel layer coatings [6].

The highest piezoelectric and dielectric responses are obtained for PZT stoichiometry close to the morphotropic phase boundary (Zr/Ti ratio 52/48) [7]. Processing conditions can be adjusted to optimize the electrical and dielectric properties [8]. The key electrical and mechanical functional properties can be further tuned by doping [9]. For example, ultrasonic motors require low dielectric losses and high mechanical quality factor [10]. On the other hand, the high piezoelectric response needed for sensors and actuators can be achieved by donor doping, for example with Nb^{5+} which increases the dielectric constant and the piezoelectric coefficient[11, 9]. Decoupling capacitors also require a high breakdown field. Nb doping increases the remanent polarization in PZT thin films [12]. Finally, dipolar defects formed on doping may modify the internal bias field and therefore the ferroelectric imprint, i.e. the displacement of the P-E hysteresis curve along the electric field axis [11].

Fortunately, PZT has a wide range of isomorphism, allowing both A and B site doping. Donor doping can be achieved by substituting the A-sites of Pb^{2+} with La^{3+} or substituting the B-sites of Zr^{4+} and Ti^{4+} with Nb^{5+}, however, it is not clear if both A and B site doping lead to similar improvements in, for example, the dielectric constant. Donor doping also modifies the microstructure, enhancing the granularity and therefore barriers to current flow, reducing film leakage [13].

The role of dopants on the chemistry and some of the consequences on the electrical properties have been studied [14, 15]. Although dopant induced tuning of the functional properties of PZT films is now well established, the correlation of those properties with the local defect chemistry and band bending is less well understood and is often model dependent, based on electrical measurements. In particular, direct evidence of how the doping induced defect chemistry modifies the electrical

Email address: nick.barrett@cea.fr (Nicholas Barrett)

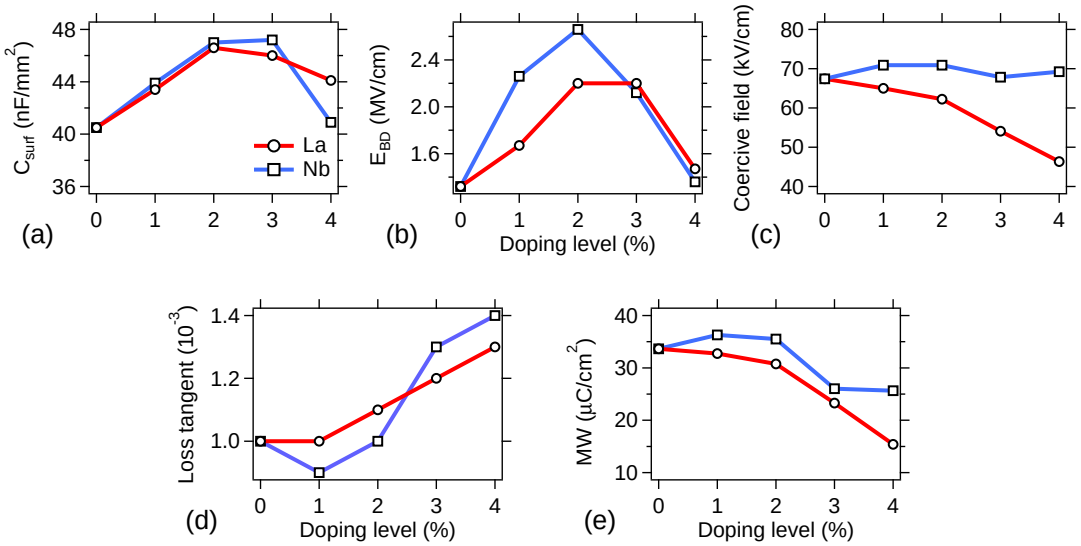

Figure 1: (a) Surface capacitance (C_{surf}) (b) breakdown field (E_{BD}) (c) modulus of coercive field ($2|E_C| = |E_{+C}| + |E_{-C}|$), (d) high field loss tangent, tan δ, and (e) memory window MW = $2|P_R|$as a function of La and Nb doping.

properties is lacking.

Dopant interaction with existing point defects such as oxygen vacancies ($V_O^{\cdot\cdot}$) should be considered. In Kröger-Vink notation, $V_O^{\cdot\cdot}$ represents a doubly positively charged oxygen vacancy resulting from the removal of $\frac{1}{2}O_2$ and the transfer of the two excess electrons to neighboring cations. The addition of Nb_2O_5 brings an extra oxygen which can fill an oxygen vacancy. Nb is known to compensate $V_O^{\cdot\cdot}$ formation on thermal activation [16]. The $V_O^{\cdot\cdot}$ formation energy is lower at domain walls than in bulk domains [17]. $V_O^{\cdot\cdot}$ can pin the domain wall motion [18], increasing the coercive field, known as ferroelectric hardening. Compensation of $V_O^{\cdot\cdot}$ by donors may therefore result in softening of the ferroelectric response and a lower coercive field.

Zhu *et al* have conducted a detailed study of softening of the dielectric and electromechanical response with La and Nb donor doping [19]. The slope of the 1 kHz ac field dependence of permittivity determined from Rayleigh analysis decreases for high (4%) La and Nb doping as does the coercive field. However, the correlations with dopant chemistry were not extensively explored.

X-ray photoelectron spectroscopy (XPS) is sensitive to both the chemical state and the valence band levels. Doping shifts the electronic levels with respect to the Fermi level. Here we use high resolution, laboratory XPS to provide information on n-type donor (La on A-site, Nb on B-site) chemistry and quantify resultant changes in the band alignment. The position of the valence band maxima was determined from a linear extrapolation of the valence band leading edge to zero. Given the Al Kα photon energy (1486.7 eV), this is a reasonable approximation [20].

XPS is also very surface sensitive. With Al Kα excitation the inelastic mean free path of Pb 4f photoelectrons is 2.5 nm [21], therefore the probing depth is approximately 7.5 nm. We have chosen to study films much thinner than 1 μm typical for piezoelectric devices and with several sol-gel layers, in order to exalt the possible role of the surface and interface chemistry to which XPS is most sensitive. Thinner layers also correspond better to decoupling capacitors which require high capacitance, the minimum usable thickness being determined by the breakdown field.

The changes observed in the band alignment are consistent with the mechanisms of defect formation and compensation on donor doping and are correlated here with changes in capacitance, dielectric losses, breakdown and coercive fields.

2. Experiment

The samples were prepared at the CEA-LETI (Grenoble). The substrates are 200 mm silicon wafers. Subsequent to the substrates cleaning, a passivation SiO_2 layer is thermally grown at 1050°C in oxygen. 20 nm thick TiO_2 adhesion layer is obtained by depositing 10 nm of Ti at 350°C followed by annealing at 750°C in oxygen for 5 min. The TiO_2 is also a Pb diffusion barrier.

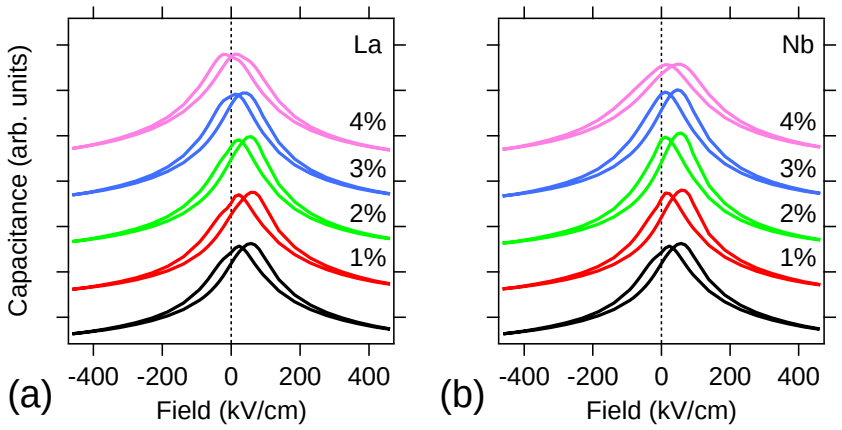

Figure 2: Capacitance-field (C-E) characteristics for (a) La (b) Nb doped samples. The C-E curves are offset vertically for clarity, from bottom to top 0, 1, 2, 3 and 4% doping, however, the relative amplitudes are exact and allow calculation of the surface capacitance. Color code of doping level: undoped (black); 1% (red); 2% (green); 3% (blue) and 4% (mauve).

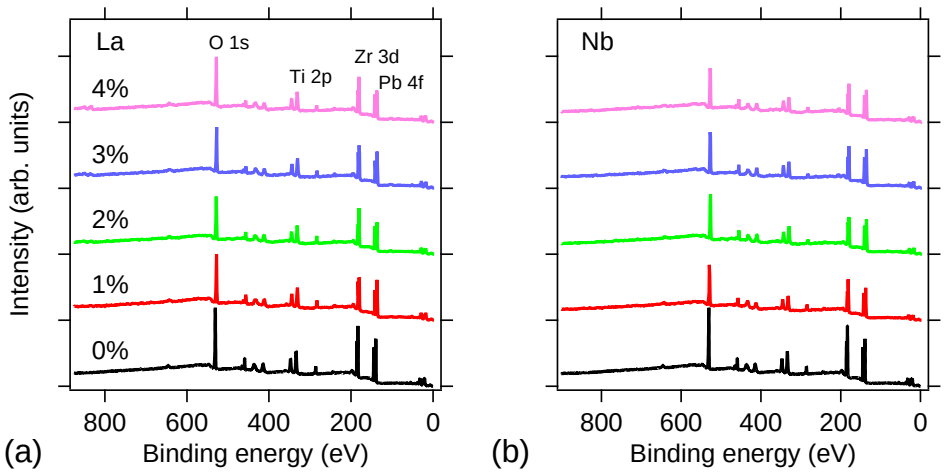

Figure 3: Survey spectra for La and Nb doped samples. Color code of doping level: undoped (black); 1% (red); 2% (green); 3% (blue) and 4% (mauve).

The 100 nm bottom Pt electrode is sputter deposited at 450°C. The details of the sol-gel layer growth are given elsewhere [22]. The sol–gel PZT films consist of multiple coating in which each coating ranges 55 nm thickness. 220 nm thick PZT films are at the morphotropic phase boundary were grown with 10% excess Pb precursor, corresponding to 4 such layers. Each layer is spun, dried at 130°C and calcinated at 360°C. A rapid thermal annealing (RTA) step is performed at 700°C for 1 min under oxygen atmosphere after calcination of the 1st and 4th layers. Doping was done using Nb_2O_5 and La_2O_3. A range of dopant concentrations (1, 2, 3 and 4 %) was introduced in the PZT precursor solutions provided by MMC (Mitsubishi Materials Corporation). For the electrical characterization, 100 nm ruthenium (Ru) top layer electrode was deposited by dc sputtering followed by photolithographic and etching to pattern a set of (80×80) μm^2 capacitors. Ru has been used as an alternative to Pt thanks to its lower cost, , its better adhesion to PZT and its propensity to be easily wet etched.

X-ray diffraction (XRD) was performed using a XPERT-PRO MRD XL from PANalytical, using Cu Kα radiation (λ = 0.15418 nm). The $\theta - 2\theta$ XRD (not shown) confirmed that all layers are predominantly (100) textured. The (111) orientation accounts for at most 15% and the (110) orientation approximately 1%. There is no obvious correlation between variation in the crystalline texture and the electrical characteristics.

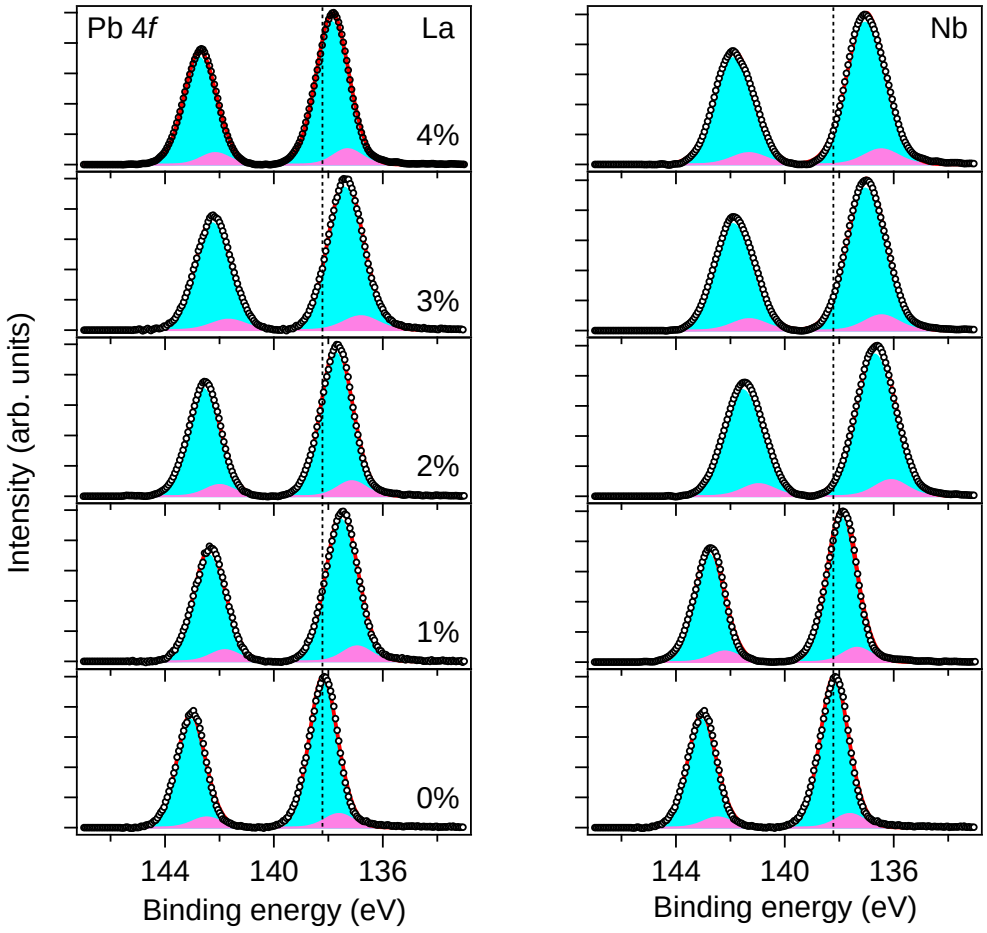

Figure 4: Pb 4f core level spectra for La (left) and Nb (right) doped samples. The spectra are fitted with two components corresponding to Pb^{2+} (cyan) and reduced Pb (magenta), shifted by 0.6 eV to lower binding energy. The bottom panels show the 4f spectrum from the undoped PZT reference film. The vertical dotted line corresponds to the BE position of the Pb^{2+} component in undoped PZT. The intensity maximum of each spectrum is normalized to unity to better evidence the band bending with doping.

Metal-ferroelectric-metal (MFM) structures with Ru electrodes were used for the electrical characterization. A HP4284A Agilent capacitance meter was used for the capacitance (C_{surf}) and dielectric loss measurement ($\tan\delta$). Measurements were carried out at 10 kHz. C_{surf} was deduced from the characteristic, capacitance-field (C-E) butterfly loops. E_{BD} was measured using Linear Ramp Voltage Stress test (with $\Delta V = 0.5$ V and $\Delta t = 0.5$ s) and Weibull statistical analysis [6]. Current as a function of voltage (I-V) were measured by using a Keithley 2400 source meter unit interfaced with a computer to perform the measurement and record data. With an appropriate trigger on the current, the voltage at which the capacitor has shorted can be detected and recorded. Short circuit is defined for an abrupt current increase, typically greater than a decade in a single voltage step. The criterion of the short circuit chosen for a capacitor of size $(80 \times 80)\ \mu m^2$ is 1 mA. As the breakdown field follows a probability law (Weibull statistical analysis), by cumulating short circuit data over 90 capacitors tested per wafer, the repartition function can be fitted and breakdown voltage can be extracted. Polarization-field (P-E) hysteresis loops were recorded using ferroelectric test module TF Analyzer 2000 from aixACCT, allowing extraction of E_C, the coercive field and MW, the memory window, defined as $(2|P_R|)$.

XPS analysis was carried out at a base pressure 5×10^{-8} Pa in a Multiprobe system (ScientaOmicron) fitted with a monochromatized Al Kα source (1486.7 eV) and a 128-channel, parallel detection Argus electron analyzer. Spectra were acquired at normal emission. The samples were mounted with double-sided conductive

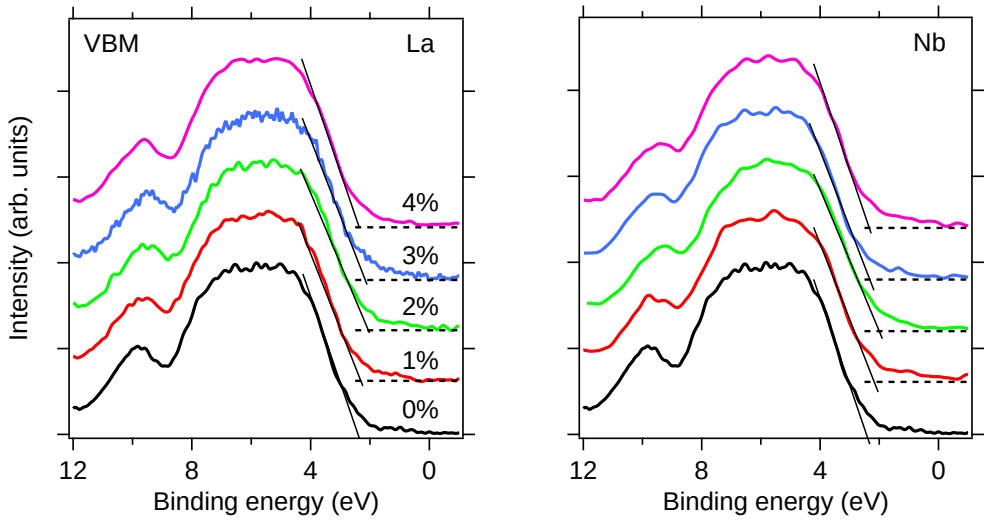

Figure 5: Valence band spectra for La (left) and Nb (right) doped samples. The linear extrapolation to determine the valence band maxima are shown as solid black lines, the baseline as dotted lines.

tape onto the metallic sample holder. We checked that this mounting was electrically equivalent to grounding the PZT surface with silver paste.

The overall energy resolution (X-ray source bandwidth and spectrometer broadening) was 0.27 eV for the core-level spectra. The binding energy scale was calibrated using the C 1*s* binding energy. CasaXPS software was used for data analysis (N. Fairley, http://www.casaxps.com/). Shirley background and a pseudo-Voigt peak shape model in the form of a Gaussian/Lorentzian product function with 30% Lorentzian character were used for the curve fitting process. The full-width at half maximum (FWHM) for each given emission line was constant.

3. Results

3.1. Electrical characterization

Figure 1 summarizes the electrical characterization of the MFM structures as a function of La and Nb doping. Figure 1a shows the maximum surface capacitance, C_{surf}, Fig. 1b the the breakdown field, E_{BD} and Fig. 1c the modulus of the coercive field, $|E_C|$. The results of the undoped PZT film are included for reference.

The surface capacitance increases from the undoped PZT value of 40.5 nF/mm^2 to a maximum of 46-47 nF/mm^2 between 2 and 3% doping.

E_{BD} also increases, reaching a maximum between 2 and 3% doping. Therefore, donor doping initially results in reduction of possible breakdown paths or mechanisms in the PZT for moderate doping levels. Indeed, breakdown paths are often associated with $V_O^{\cdot\cdot}$ percolation [23, 24]. In contrast, above 3% doping, E_{BD} decreases sharply. This may reflect that while moderate doping compensates $V_O^{\cdot\cdot}$, higher doping levels give rise to a more classical type n doping, creating higher leakage and therefore reducing the breakdown field. It may also be that saturation doping levels have been reached giving rise to phase separation. The possibility of the latter is discussed below.

The modulus of E_C, the coercive field, defined by $2|E_C| = |E_C^+| + |E_C^-|$, is almost constant for Nb doping, but decreases with La doping (Fig. 1c). This is the major electrical difference between La and Nb doping. Although both La and Nb doping can compensate $V_O^{\cdot\cdot}$ on defect activation, only La doping appears to soften the ferroelectric state. Zhu *et al* also observed a decrease in coercive field with La doping, although on thicker films (2 μm) which may explain why the reduction was less marked than here [19]. Softening often results from domain wall unpinning. As both La and Nb doping compensate $V_O^{\cdot\cdot}$, it is not clear why the A-site doping results in a stronger decrease of E_C. One possibility is that A-site La doping could fully compensate $V_{Pb}^{''}$-$V_O^{\cdot\cdot}$ defect dipoles. The relatively high Born effective charge of Pb in PZT may provide one clue as to the large change in E_C on La A-site doping[25]. However, ab-initio calculations should be performed to specifically look at the role of dopant-related local charge and defects on the ferroelectric softening. The loss tangent and memory window as a function of doping are reported in Fig. 1d and e. The high field losses increase from 0.010 to 0.013

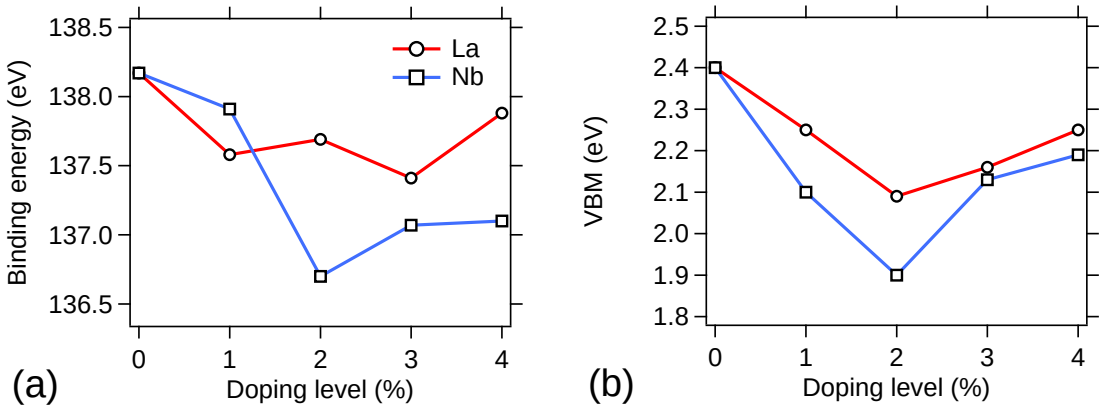

Figure 6: (a) Pb $4f_{7/2}$ core level shift as a function of La (red curve, open circles) and Nb (blue curve, open squares) doping. 2% La, Nb doping results in a shift towards the Fermi level, consistent with $V_O^{\cdot\cdot}$ annihilation. Above 2% Nb and 3% La concentration, the band bending is away from the Fermi level, consistent with additional n-type doping. (b) Valence band maximum (VBM) as a function of doping.

with La doping and from 0.009 to 0.014 with Nb doping. They are nevertheless low, showing that the films are not leaky, despite doping up to 4%. The memory window narrows significantly above 2% doping, particularly for La doping, falling to half its maximum value.

Figure 2 shows the capacitance-field characteristics for (a) La and (b) Nb doped samples. The characteristic butterfly loops are observed and doping up to 2% increases the imprint slightly with respect to the undoped PZT.

The results show that two parameters, C_{surf} and E_{BD} improve to optimal values between 2 and 3% donor doping levels. Beyond this threshold, the capacitive characteristics start degrading. The coercive field decreases with increasing La doping. The quantitative results for the maximum surface capacitance, breakdown field, coercive field, high field loss tangent and memory window as a function of La and Nb doping as well as the valence band maxima, discussed below, are reported in Fig. 1.

3.2. X-ray photoelectron spectroscopy

The XPS survey spectra for La and Nb doping are shown in Fig. 3. They are virtually identical for all dopants apart from the specific dopant core level lines. Thus, the overall PZT chemistry is not affected by doping and we do not expect any major chemically induced change in the electrical characteristics. However, subtle shifts in the electronic levels are observed as a function of doping. We use the well-defined Pb 4f core level emission to follow the doping-induced shifts of the energy band diagram.

The Pb 4f spectra for the La and Nb doped PZT are shown in Fig. 4a and b. The binding energy scale has been calibrated with respect to the C 1s emission at 285 eV. For comparison, the undoped PZT spectrum (black curve) is included in each panel. The spectra have two components, the main one due to Pb^{2+} in PZT and a low binding energy (LBE) component, shifted by 0.6 eV with respect to the main peak. The LBE component accounts for 10% of the total intensity and represents reduced Pb. Hard X-ray photoemission suggests that it is at least partly intrinsic to the sol-gel PZT layers [26]. No evolution of this component is observed during data acquisition time, therefore it is not due to interaction with Al Kα radiation. Upwards band bending towards the Fermi level is observed for both donor dopants, it is more marked for the Nb dopant (site B) than for La dopant (site A). The band bending reaches a maximum for 2% Nb and between 2 and 3% for La. For doping above 2%, the low binding energy component increases in intensity and is responsible for the increase in the width of the Pb 4f manifold.

Figure 5 presents the valence band spectra and the method used to determine the valence band maxima (VBM) for the La and Nb doped samples. The VBM is determined from the intersection of a linear extrapolation of the valence band leading edge (solid line) with the baseline (dotted line). With doping the VBM first moves up towards the Fermi level then, above 2%, shifts in the opposite direction. The quantitative band bending, as measured from the positions of the main Pb 4f component and the VBM, is plotted in Fig. 6.

Figure 6a plots the measured Pb $4f_{7/2}$ band shifts as a function of doping level. Nb is a donor, providing one electron per dopant on B-sites. From basic semiconductor band theory one would expect the electron energy levels to shift away from the Fermi level, i.e. to higher binding energy for n-type doping. However, Nb in the

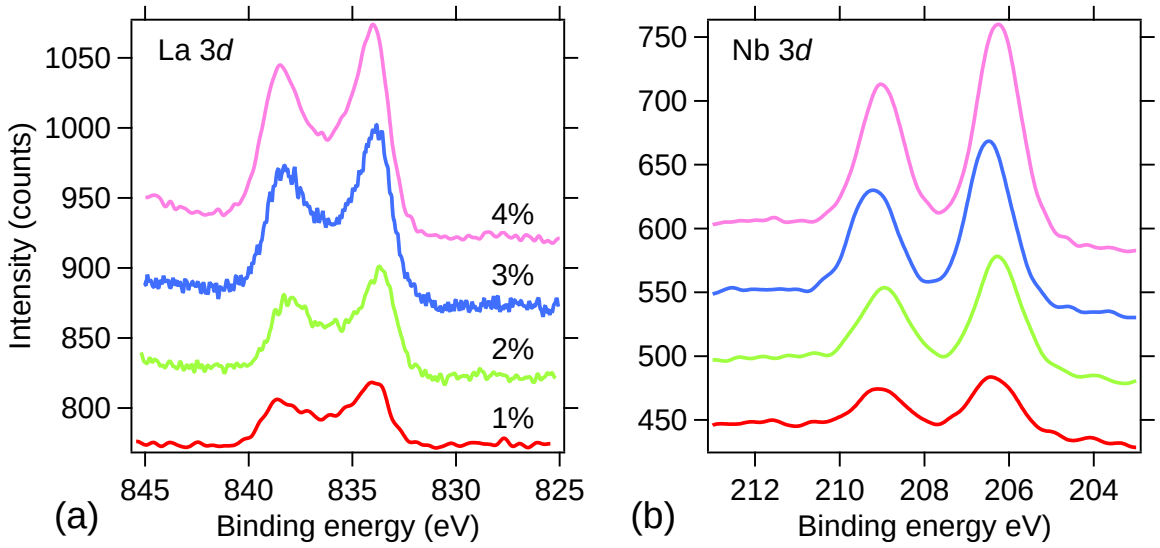

Figure 7: (a) La and (b) Nb 3d core level spectra for, from bottom to top, 1,2,3 and 4% doping level. The spectra are offset vertically for clarity. Color code as in Fig. 3

form of Nb_2O_5 also brings in extra oxygen on defect activation and reduces the $V_O^{\cdot\cdot}$ concentration following the reaction $Nb_2O_5+V_O \rightarrow 2Nb_{Ti}+5O_O$ [16, 27, 28]. Since each $V_O^{\cdot\cdot}$ provides two electrons to the lattice, the reduction in $V_O^{\cdot\cdot}$ on Nb doping initially reduces the effective n-type doping of the PZT. The reduction in the intrinsic $V_O^{\cdot\cdot}$ concentration should also result in enhancement of the dielectric constant which is indeed what we observe for 2-3% La and Nb doping. The La-induced shifts are smaller than those due to Nb doping. This may be because $V_O^{\cdot\cdot}$ interact more strongly with B-site than with A-site cations.

The same trends are observed in the position of the valence band maxima (Fig. 6b) but the shifts are smaller than those observed on the core levels. This is surprising since doping should induce a rigid shift in both core levels and the VBM. As for the Pb 4f core level the shift towards the Fermi level is a maximum at 2% La and Nb doping, however, the magnitude is smaller, possibly because of the difficulty in localizing the VBM in the presence of gap states due, for example, to residual carbon contamination. Figure 6b shows that La and Nb doping increases significantly the Schottky barrier height for electrons compared with that of undoped PZT.

To address the possibility of dopant phase separation, Fig. 7 shows the La and Nb 3d core level spectra. The intensity increases with doping, confirming the nominal doping levels. Based on the inelastic mean free paths (IMFP) generated by the QUASES-IMFP-TPP2M software [29], bulk escape depths from La and Nb 3d core levels are estimated to be 6.3 and 6.8 nm respectively. The probing depths are therefore close to that of the Pb $4f_{7/2}$ emission. The lineshapes do not change with doping, therefore the chemical state is constant and there is no evidence of phase separation due to dopants reaching the solubility limit. The differences in the electrical characteristics indeed appear to be linked to the interactions between the La and Nb dopants with existing defects ($V_O^{\cdot\cdot}$) and to doping induced band shifts, rather than to changes in local dopant chemistry.

Figure 8 shows the band lineup deduced from the VBM data for Nb doping reported in Fig. 6b and assuming a 3.4 eV band gap [30]. The valence band maximum (VBM) shifts towards the Fermi level up to 2% doping, opposite to what would be expected from simple n-type doping. For higher doping the VBM moves down away from the Fermi level, suggesting that the intrinsic $V_O^{\cdot\cdot}$ have been compensated by the additional oxygen supplied by Nb_2O_5 and that further doping gives a characteristic n-type shift away from the Fermi level as reported for La and Nb donor doping levels greater than 4% [13]. The donor induced band bending is stronger for Nb than for La, also reported by Zou *et al* [13]. Each Nb_2O_5 will dope two TiO_2 sites and provides one more oxygen than the stoichiometric PZT can absorb. As a result, a $V_O^{\cdot\cdot}$ is filled, removing two electrons donated by the $V_O^{\cdot\cdot}$. The result is therefore a displacement of the electron bands towards the Fermi level, usually associated with p-type doping. A similar schematic can be drawn for La doping using the values in Fig. 6.

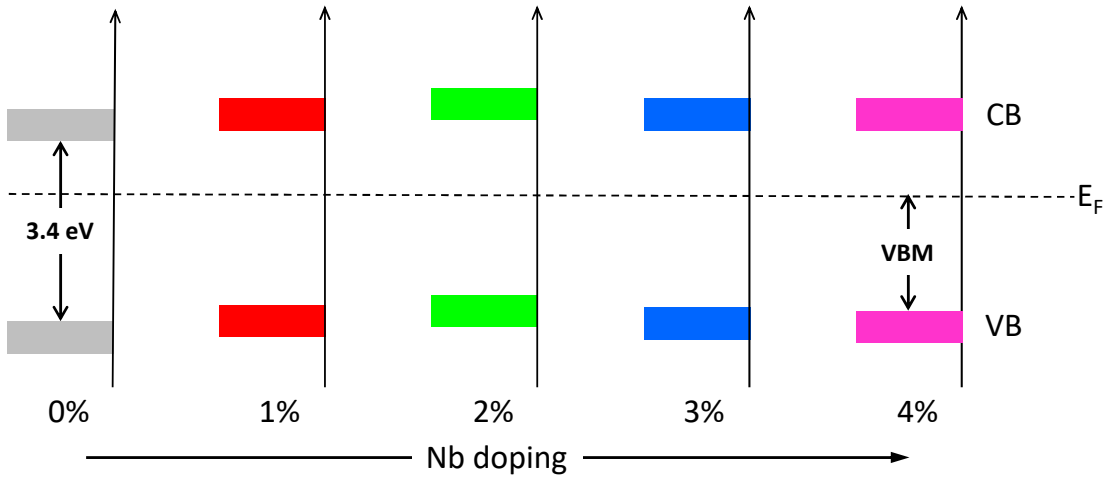

Figure 8: Schematic of band lineup variation as a function of Nb doping. The valence band maximum is closest to the Fermi level for 2% doping. Color code is as in Fig. 3.

4. Discussion

We have measured the band shifts in PZT induced by donor (La, Nb) dopants. Doping leads to upward band bending towards the Fermi level due to filling of $V_O^{\cdot\cdot}$ by the extra oxygen associated with La and Nb doping on the A and B sites, respectively. The band bending is stronger for Nb than La doping, possibly due to the stronger interaction of $V_O^{\cdot\cdot}$ with B-site cations. Donor doping up to 2-3% of both A and B sites leads to improved dielectric constant and breakdown field but the dielectric losses at high field increase slightly. This may be related to an additional conduction mechanism which becomes possible once the $V_O^{\cdot\cdot}$ have been compensated by the oxygens supplied by the La_2O_3 or Nb_2O_5. Higher, randomly distributed, n-type doping creates new loss mechanisms which may also reduce the imprint [31]. The increase in the overall width of the Pb 4f peaks above 2% doping is consistent with the availability of free electrons, which may reduce additional Pb ions. Additional conducting paths will increase leakage and higher current would dissipate more thermal energy and may favour electrothermal breakdown. The doping dependance of C_{surf} is consistent with the evolution in $V_O^{\cdot\cdot}$ concentration because domain wall pinning decreases as the $V_O^{\cdot\cdot}$ concentration decreases.

The decrease in the coercive field observed for 4% La doping was also observed for much thicker Nb- and La-doped films with similar doping level [19]. The same authors reported a decrease in the slope of the permittivity with ac field for 4% La and Nb doping, as measured by Rayleigh analysis. Our results suggest that at 3% doping, $V_O^{\cdot\cdot}$ have been compensated by La_2O_3 and Nb_2O_5, freeing the domain wall movement. Further doping introduces more free charge via classical n-type doping and these additional charges can perturb the domain wall movement, reducing the slope of the permittivity.

The reduction in the valence band offset at 2% doping may also result in the suppression of defect induced gap states and inhibit defect development. The shift of the VBM for 2% doping corresponds to a higher Schottky barrier height for electrons. The maximum in the breakdown field might therefore be correlated with both $V_O^{\cdot\cdot}$ compensation, reducing conductivity, and the band shift, increasing the Schottky barrier height.

Both dopants give a stronger imprint than in the undoped PZT up to 2-3% doping, consistent with the formation of complex defects on doping. The main difference observed between A-site (La) and B-site (Nb) doping is in the coercive field. La doping softens considerably the ferroelectric state, reducing significantly the coercive field whereas Nb leaves the coercive field unchanged, suggesting that domain unpinning is mostly done by compensating $V_O^{\cdot\cdot}$ through A-site doping. Band bending, on the other hand, is stronger for the Nb doping. Doping results in band shifts due first to $V_O^{\cdot\cdot}$ compensation and then A and B-site n-type doping. No chemical change is observed in the PZT nor in the local dopant chemistry. The improvement in the ferroelectric properties is most marked for 2% La and Nb doping.

The 20% increase in E_{BD} at 2% doping is particularly interesting from an application point of view since it may allow to use thinner films, increasing the capacitance whilst maintaining the remanent polarization at a

reasonable level compared to the undoped PZT. Higher doping considerably reduces the remanent polarization and hence the memory window.

The electrical characteristics are generally slightly better with Nb doping. However, one interesting aspect of combined A- and B-site doping might be to maintain the unit cell volume constant since the unit cell should contract on La A-site doping but expand on Nb B-site doping.

5. Conclusion

In summary, modest La and Nb doping of sol-gel PZT leads to upward band bending and filling of $V_O^{\cdot\cdot}$ by the extra oxygen associated with La_2O_3 and Nb_2O_5 on the A and B sites, respectively. Doping up to 2-3% of both A and B sites leads to improved dielectric constant and breakdown field but the dielectric losses at high field increase slightly. C_{surf} is consistent with the $V_O^{\cdot\cdot}$ concentration. We suggest that at 3% doping, $V_O^{\cdot\cdot}$ have been compensated by La_2O_3 and Nb_2O_5, freeing the domain wall movement. The Schottky barrier height for electrons increases with doping up to 2% which may also explain the maximum in the breakdown field.

The main difference observed between A and B site doping is in the coercive field and band bending. La doping softens the ferroelectric state whereas Nb leaves it unchanged, suggesting that domain unpinning is mostly done by compensating $V_O^{\cdot\cdot}$ through A-site doping. Band bending is stronger for the Nb doping. Doping results in band shifts due to $V_O^{\cdot\cdot}$ compensation up to 2-3 %. For higher doping levels more classical n-type behaviour is observed.

The complex interaction between local dopant chemistry, band shifts and ferroelectric properties revealed by electrical measurements and XPS analysis should allow optimization of PZT for a variety of applications.

6. Acknowledgments

I.G. was funded by a CEA-LETI research grant. We acknowledge the support from the Nanocharacterization Platform of CEA-MINATEC and from the CEA operando project. E.D. acknowledges the Luxembourg National Research Fund for its support through the project HARVESTORE (INTER/ANR/18/12618689). We thank Torsten Granzow for valuable discussions on the band line-up.

The data that support the findings of this study are available from the corresponding author upon reasonable request.

References

[1] P. Muralt, Ferroelectric thin films for micro-sensors and actuators : a, J. Micromech. MicroEng. 10 (2000) 136–146.

[2] Y. B. Jeon, R. Sood, J. H. Jeong, S. G. Kim, MEMS power generator with transverse mode thin film PZT, Sensors and Actuators, A: Physical 122 (1 SPEC. ISS.) (2005) 16–22. doi:10.1016/j.sna.2004.12.032.

[3] H. N. Al-Shareef, D. Dimos, Leakage and Reliability Characteristics of Lead Zirconate Titanate Thin-Film Capacitors, Journal of the American Ceramic Society 80 (12) (2010) 3127–3132. doi:10.1111/j.1151-2916.1997.tb03240.x.

[4] R. Moazzami, C. Hu, W. H. Shepherd, Electrical characteristics of ferroelectric PZT thin films for DRAM applications, IEEE Transactions on Electron Devices 39 (9) (1992) 2044–2049. doi:10.1109/16.155876.

[5] R. Takayama, Y. Tomita, Preparation of epitaxial Pb(ZrxTi1-x)O3thin films and their crystallographic, pyroelectric, and ferroelectric properties, Journal of Applied Physics 65 (4) (1989) 1666–1670. doi:10.1063/1.342936.

[6] I. Gueye, G. L. Rhun, O. Renault, E. Defay, N. Barrett, Electrical response of Pt/Ru/PbZr0.52Ti0.48O3/Pt capacitor as function of lead precursor excess, Appl. Phys. Lett. 111 (2017) 222902.

[7] X.-h. Du, J. Zheng, U. Belegundu, K. Uchino, Crystal orientation dependence of piezoelectric properties of lead zirconate titanate near the morphotropic phase boundary, Applied Physics Letters 72 (19) (1998) 2421–2423. doi:10.1063/1.121373.
URL http://aip.scitation.org/doi/10.1063/1.121373

[8] S. Q. Yin, A. D. Liu, Y. Y. Zhang, K. S. Venkatesh, M. Manikandan, Y. C. Shi, P. Y. Chen, M. Z. Hou, S. Y. Shang, J. Shang, X. W. Wang, Improved properties of Pb(Zr0.52Ti0.48)O3 films by hot plate annealing on LaNiO3 bottom electrode, Journal of Sol-Gel Science and Technology 96 (2020) 83–90. doi:10.1007/s10971-020-05378-w.
URL http://dx.doi.org/10.1007/s10971-020-05378-w

[9] M. D. Nguyen, T. Q. Trinh, M. Dekkers, E. P. Houwman, H. N. Vu, G. Rijnders, Effect of dopants on ferroelectric and piezoelectric properties of lead zirconate titanate thin films on Si substrates, Ceramics International 40 (1 PART A) (2014) 1013–1018. doi:10.1016/j.ceramint.2013.06.098.
URL http://dx.doi.org/10.1016/j.ceramint.2013.06.098

[10] Kenji Uchino, Piezoelectric ultrasonic motors: overview, Smart Materials and Structures 7 (3) (1998) 273. doi:http://dx.doi.org/10.1088/0964-1726/7/3/002.
URL http://stacks.iop.org/0964-1726/7/i=3/a=002

[11] T. Haccart, D. Remiens, E. Cattan, Substitution of Nb doping on the structural, microstructural and electrical properties in PZT films, Thin Solid Films 423 (2) (2003) 235–242. doi:10.1016/S0040-6090(02)01045-3.

[12] K. W. Kwok, R. C. W. Tsang, H. L. W. Chan, C. L. Choy, Effects of niobium doping on the piezoelectric properties of sol-gel derived lead zirconate titanate films, Journal of Applied Physics 95 (3) (2004) 1372–1376. doi:10.1063/1.1635968.

[13] Q. Zou, H. Ruda, B. G. Yacobi, M. Farrell, Microstructural characterization of donor-doped lead zirconate titanate films prepared by sol-gel processing, Thin Solid Films 402 (1-2) (2002) 65–70. doi:10.1016/S0040-6090(01)01708-4.

[14] S. B. Desu, D. A. Payne, Interfacial Segregation in Perovskites: II, Experimental Evidence, Journal of the American Ceramic Society 73 (11) (1990) 3398–3406. doi:10.1111/j.1151-2916.1990.tb06467.x.

[15] S. B. Desu, D. A. Payne, Interfacial Segregation in Perovskites: I, Theory, Journal of the American Ceramic Society 73 (11) (1990) 3391–3397. doi:10.1111/j.1151-2916.1990.tb06466.x.

[16] J. F. Chang, S. B. Desu, Effects of dopants in PZT films, Journal of Materials Research 9 (4) (1994) 955–969. doi:10.1557/JMR.1994.0955.

[17] L. He, D. Vanderbilt, First-principles study of oxygen-vacancy pinning of domain walls in PbTiO$_3$, Physical Review B 68 (13) (nov 2003). doi:10.1103/PhysRevB.68.134103.
URL http://link.aps.org/doi/10.1103/PhysRevB.68.134103

[18] S. J. Brewer, S. C. Williams, C. Z. Deng, A. B. Naden, S. M. Neumayer, B. J. Rodriguez, A. Kumar, N. Bassiri-Gharb, Functional and structural effects of layer periodicity in chemical solution-deposited Pb(Zr,Ti)O3 thin films, Journal of the American Ceramic Society 100 (12) (2017) 5561–5572. doi:10.1111/jace.15057.

[19] W. Zhu, I. Fujii, W. Ren, S. Trolier-Mckinstry, Domain wall motion in A and B site donor-doped Pb (Zr 0.52 Ti 0.48) O 3 films, Journal of the American Ceramic Society 95 (9) (2012) 2906–2913. doi:10.1111/j.1551-2916.2012.05243.x.

[20] S. Chambers, T. Droubay, T. Kaspar, M. Gutowski, M. van Schilfgaarde, Accurate valence band maximum determination for SrTiO3(001), Surface Science 554 (2-3) (2004) 81–89. doi:10.1016/j.susc.2004.02.021.
URL http://linkinghub.elsevier.com/retrieve/pii/S0039602804001815

[21] H. Shinotsuka, S. Tanuma, C. J. Powell, D. R. Penn, Calculations of electron inelastic mean free paths . X . Data for 41 elemental solids over the 50eV to 200keV range with the relativistic full Penn algorithm, Surface Interface Analysis 47 (May) (2015) 871–888. doi:10.1002/sia.5789.

[22] W. D. Yang, PZT/PLZT ceramics prepared by hydrolysis and condensation of acetate precursors, Ceramics International 27 (4) (2001) 373–384. doi:10.1016/S0272-8842(00)00091-2.

[23] R. Waser, M. Klee, Theory of conduction and breakdown in perovskite thin films, Integrated Ferroelectrics 2 (1-4) (1992) 23–40. doi:10.1080/10584589208215729.
URL https://doi.org/10.1080/10584589208215729

[24] R. Waser, M. Aono, Nanoionics-based resistive switching memories, Nature Materials 6 (11) (2007) 833–840 LA – en. doi:10.1038/nmat2023.
URL http://www.nature.com/nmat/journal/v6/n11/full/nmat2023.html

[25] P. Ghosez, J. Michenaud, X. Gonze, Dynamical atomic charges: The case of compounds, Physical Review B - Condensed Matter and Materials Physics 58 (10) (1998) 6224–6240. arXiv:9805013, doi:10.1103/PhysRevB.58.6224.

[26] I. Gueye, G. Le Rhun, O. Renault, D. Cooper, D. Ceolin, J.-P. Rueff, N. Barrett, Operando hard X-ray photoelectron spectroscopy study of the Pt/Ru/PbZr<inf>0.52</inf>Ti<inf>0.48</inf>O<inf>3</inf>interface, Applied Physics Letters 111 (3) (2017). doi:10.1063/1.4993909.

[27] C. Ruangchalermwong, J. F. Li, Z. X. Zhu, S. Muensit, Phase transition and electrical properties of highly [1 1 1]-oriented and niobium-modified Pb(ZrxTi1-x)O3 thin films with different Zr/Ti ratios, Journal of Physics D: Applied Physics 41 (22) (2008). doi:10.1088/0022-3727/41/22/225302.

[28] C. Ruangchalermwong, J. F. Li, Z. X. Zhu, F. Lai, S. Muensit, Enhanced ferro- and piezoelectric properties in (100)-textured Nb-doped Pb(ZrxTi1 - x)O3 films with compositions at morphotropic phase boundary, Thin Solid Films 517 (24) (2009) 6599–6604. doi:10.1016/j.tsf.2009.04.045.
URL http://dx.doi.org/10.1016/j.tsf.2009.04.045

[29] S. Tanuma, C. J. Powell, Electron Inelastic Mean Free Paths., Surface and Interface Analysis 21 (September 1993) (1993) 165–176.

[30] S. Samanta, V. Sankaranarayanan, K. Sethupathi, Band gap, piezoelectricity and temperature dependence of differential permittivity and energy storage density of PZT with different Zr/Ti ratios, Vacuum 156 (May) (2018) 456–462. doi:10.1016/j.vacuum.2018.08.015.
URL https://doi.org/10.1016/j.vacuum.2018.08.015

[31] H. Tamura, Microwave dielectric losses caused by lattice defects, Journal of the European Ceramic Society 26 (10-11) (2006) 1775–1780. doi:10.1016/j.jeurceramsoc.2005.09.080.